

Journal of Materials Chemistry A

Accepted Manuscript



This is an *Accepted Manuscript*, which has been through the Royal Society of Chemistry peer review process and has been accepted for publication.

Accepted Manuscripts are published online shortly after acceptance, before technical editing, formatting and proof reading. Using this free service, authors can make their results available to the community, in citable form, before we publish the edited article. We will replace this *Accepted Manuscript* with the edited and formatted *Advance Article* as soon as it is available.

You can find more information about *Accepted Manuscripts* in the [Information for Authors](#).

Please note that technical editing may introduce minor changes to the text and/or graphics, which may alter content. The journal's standard [Terms & Conditions](#) and the [Ethical guidelines](#) still apply. In no event shall the Royal Society of Chemistry be held responsible for any errors or omissions in this *Accepted Manuscript* or any consequences arising from the use of any information it contains.

Cite this: DOI: 10.1039/c0xx00000x

ARTICLE TYPE

www.rsc.org/xxxxxx

Three-dimensionally ordered porous TiNb₂O₇ nanotubes: superior anode material for next generation hybrid supercapacitors

Hongsen Li, Laifa Shen, Jie Wang, Shan Fang, Yingxia Zhang, Hui Dou and Xiaogang Zhang*

Received (in XXX, XXX) Xth XXXXXXXXX 20XX, Accepted Xth XXXXXXXXX 20XX

DOI: 10.1039/b000000x

Hybrid supercapacitors are one very appealing power source with high energy density and power density because they employ both the merits of lithium ion batteries and supercapacitors. To balance such hybrid systems, the rate for the redox component must be substantially comparative to the levels of the double layer process. Taking this issue for the intercalation electrode material TiNb₂O₇, we have used facile steps electrode design consisting of the physically assisted template infusion of Ti-Nb sol into the pores of AAO followed by *in situ* convention into porous TiNb₂O₇ nanotubes within the AAO walls under calcinations, and finally making those templates dissolve away. Using such electrode as battery type anode and graphene grass electrode as capacitor type cathode, we successfully constructed a novel hybrid supercapacitor. Within a voltage range of 0-3 V, a high energy density of ~74 Wh kg⁻¹ is achieved and it could maintain as much as ~34.5 Wh kg⁻¹ at a power of 7500 W kg⁻¹. The present research demonstrates a feasible and effective strategy to solve the high energy density and high power density uncoupled difficulty for hybrid supercapacitors.

Introduction

Advanced energy storage devices are urgently needed to satisfy the rapidly increasing demands for new applications that require high energy, high power, and cost-effective energy storage systems (ESSs).¹⁻⁸ In this context, lithium ion batteries (LIBs) are considered to be very attractive energy storage devices, as they have high energy densities (150-200 Wh·kg⁻¹) through Faradaic lithium insertion reactions. However, LIBs are still not capable of delivering high power densities comparable to those of supercapacitors which is mainly due to intrinsically slow charge transfer and ion diffusion occurring at bulk electrode materials. This drawback restricts the use of LIBs mainly to large-scale applications, and the cost is too high.⁹⁻¹² Alternatively, supercapacitors exhibit competitive advantages such as the highest known power capability (2-5 kW kg⁻¹) and long cycle life (up to 10⁴ cycles), owing to non-Faradaic surface reactions through accumulation of ions on the electrode surface. However, since supercapacitors generally have low energy densities (3-6 Wh kg⁻¹), their uses are limited and cannot fully meet performance demands required in high energy density storage devices.¹³⁻¹⁶ Thus, in order to bridge the gap to optimize the energy and power densities, new energy storage devices necessitate both the attributes of lithium ion batteries, allowing high energy density, and the characteristics of electrochemical capacitors of fast charge discharge rates.¹⁷⁻²¹

Recently, such hybrid energy devices with characteristics employing both the system of a battery type component (energy source, anode) and a capacitor type component (power source, cathode) has been proposed.¹⁵ The battery type component similar to that in LIBs undergoes a redox reaction, providing the necessary energy density, while the capacitor type component like the electrical double layer capacitors (EDLC) involve anionic double layer formation across the electrode/electrolyte interface, delivering high power densities.²² The hybrid supercapacitors could certainly overcome the energy density limitation of conventional electrochemical capacitors, producing a larger working voltage and capacitance. However, the primary drawback of these kinds of devices is that the power and energy performances are decoupled. Due to the response is dominated by capacitor type component at high current densities, the energy density of the hybrid device is considerably diminished.¹¹

To resolve the aforementioned challenge, a hybrid electrode, which could adopt fast surface electrode reactions while maintaining high energy density, is necessary.²³⁻²⁶ Fortunately, the energy storage technologies have been advanced which benefit from the transforming from conventional to nanostructured electrodes. For battery type electrodes, TiNb₂O₇ has been recognized as a promising insertion host due to its high theoretical capacity (~2 times higher than Li₄Ti₅O₁₂), excellent reversibility, good cyclability, and high safety.²⁷⁻³⁵ However, due to the intrinsic low electrical conductivity and sluggish solid-state

diffusion of Li ions, the bulk TiNb_2O_7 electrode suffers from kinetic problems resulting in the capacity fading and inferior high rate property. How to design and fabricate an advanced architecture to get the fastest kinetics in order to fulfill the desired performance remains a challenge. Among the various nanostructures, hollow nanotubes structure had attracted extensive interest because of their unique chemical and physical characteristics.³⁶⁻³⁸ In the ordinary batteries, owing to the high surface energy, nanomaterials are often self-aggregated, which reduces the effective contact areas of active materials, conductive additives, and electrolyte. However, the powerful hollow nanotubes architecture can keep the effective contact areas large and fully realize the advantage of active materials at nanometer scale.^{39, 40} For supercapacitor type electrodes, the specific capacity of the most widely used activated carbon (AC) is relatively low and decreases sharply with increasing current densities. Therefore, researches should be focused on searching alternative carbonaceous materials with high electrical conductivity and large specific surface area. Recently, Chen *et al.* reported that the 3D porous graphene based carbon materials could be used as a promising cathode material for a hybrid supercapacitor and enhanced electrochemical were obtained simultaneously.¹⁰

In present work, we designed a three-dimensionally (3D) well-defined uniform anode electrode structure, constituting of vertical arrays of hollow TiNb_2O_7 nanotubes with abundant mesoporous pores inside. The advanced architecture of TiNb_2O_7 result in superior electrochemical capacitive properties including high specific capacity, excellent rate capability, significantly enhanced cycling performance. Furthermore, a hybrid supercapacitor which is based on an anode electrode of TiNb_2O_7 nanotubes and a cathode electrode of graphene grass was fabricated. The novel hybrid supercapacitor system are capable of delivering a high energy density of $\sim 74 \text{ Wh kg}^{-1}$, and it can even maintain approximately 34.5 Wh kg^{-1} at a 33.5 seconds charge/discharge rate. More importantly, the energy density is able to stabilize at $\sim 43.8 \text{ Wh kg}^{-1}$ at 1 A g^{-1} after 3000 cycles, corresponding to 0.0062% fading per cycle, exhibiting an ultra-long cycle life.

Experimental

Materials synthesis

Synthesis of 3D ordered porous TiNb_2O_7 nanotubes (3D-O-P-TNO): Anodic aluminum oxide (AAO) templates (Whatman, 13 mm in diameter, 0.2 μm pore diameter, and 60 μm template thickness) were used as the template for making TiNb_2O_7 nanotubes. In a typical procedure, 10 mmol niobium chloride (NbCl_5 ; 99.99%, Aladdin) and 5 mmol titanium (IV) isopropoxide ($\text{C}_{12}\text{H}_{28}\text{O}_4\text{Ti}$, TIP; 97%, Aladdin) were added to 5 mL ethanol to prepare a Ti-Nb sol. Then ten AAO templates were dipped into a moderate volume of the Ti-Nb sol for 20 min before they were taken out for vacuum drying at 35 $^\circ\text{C}$ for 10 h. The AAO/Ti-Nb composites were converted to AAO/ TiNb_2O_7 by calcining at 700 $^\circ\text{C}$ for 2 h under a slow flow of Ar gas. After cooling down, the AAO templates were removed by immersing the as-prepared sample in a solution of 2 M H_3PO_4 for 12 h. For comparison, bulk TiNb_2O_7 (TNO) was synthesized using the same procedure without the assistance of AAO template.

Synthesis of graphene grass: Graphite oxide (GO) was prepared from natural graphite flakes using a modified Hummers method^{41, 42}. The graphene grass was prepared by a combination of hydrothermal assembly and freeze-drying process. Typically, 50 mL GO (2 mg mL^{-1}) solution mixed with 10 mL hydrazine hydrate was dispersed in a beaker by sonication for 2 h. Then the solution were transferred to 80 mL Teflon-lined stainless steel autoclave and kept in an electric oven at 100 $^\circ\text{C}$ for 10 h. Finally, the as-prepared sample was cleaned and freeze-dried overnight, followed by vacuum drying at 60 $^\circ\text{C}$ for 5 h.

Materials characterization

The crystal structure of the obtained samples was characterized by X-ray diffraction (XRD) (Bruker D8 advance) with Cu Ka radiation. Schematic illustrations of the crystal structures were drawn using the program VESTA⁴³. Microstructural properties were determined using transmission electron microscopy (TEM) (TEM, FEI, Tecnai-20), high-resolution transmission electron microscopy (HRTEM, JEOL JEM-2010), and field-emission scanning electron microscopy (FESEM, HITACHI S-4800). The N_2 adsorption/desorption were determined by Brunauer-Emmett-Teller (BET) measurements using an ASAP-2010 surface area analyzer.

Electrochemical Measurement

Electrochemical evaluations were performed by galvanostatic cycling in a CR2016-type coin cell. For the 3D-O-P-TNO electrode, a mixture of containing of 80 wt.% active materials, 10 wt.% carbon black, and 10 wt.% polyvinylidene fluoride were dissolved in N-methyl pyrrolidinone, and pasting the mixture on a copper-foil current collector. The preparation of graphene grass electrode was as same as that of 3D-O-P-TNO electrode, whereas the aluminium foil was used as current collector. In the aforesaid electrode, lithium metal was used as counter and reference electrode and polypropylene (PP) film as separator. The electrolytes were 1 mol L^{-1} LiPF_6 solution in a 1 : 1 (V : V) mixture of ethylene carbonate (EC) and dimethyl carbonate (DMC). All the Test cells assembly process was in an argon-filled glove box. In these electrochemical measurements of hybrid supercapacitor, 3D-O-P-TNO electrode and graphene grass electrode were used as negative electrode and positive electrode, respectively, using the same organic electrolyte. In this hybrid supercapacitor, the mass ratio of positive electrode/negative electrode was 5 : 1. Galvanostatically charge/discharge experiments were performed at different current densities using a CT2001A cell test instrument (LAND Electronic Co.).

Results and discussion

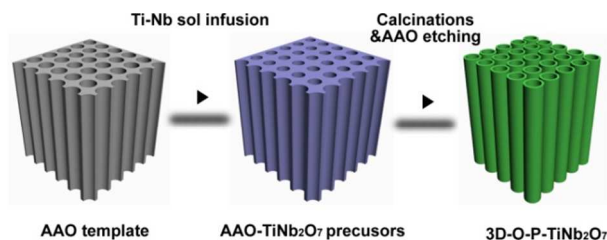


Fig. 1. Schematic representation of the fabrication process for 3D-O-P-TNO.

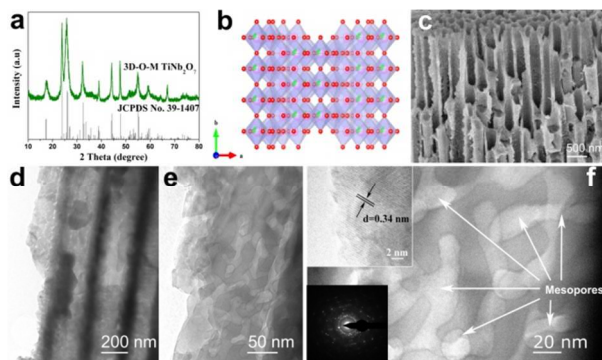


Fig. 2. (a) XRD patterns of 3D-O-P-TNO; (b) the crystal structure of TiNb_2O_7 , viewed along the c -axis; (c) SEM image of 3D-O-P-TNO; (d) TEM image and (e, f) HRTEM images of 3D-O-P-TNO.

5

Briefly, Fig. 1. schematically illustrates the fabrication steps of 3D-O-P-TNO. The Ti-Nb sol was firstly prepared by dissolving NbCl_5 and $\text{C}_{12}\text{H}_{28}\text{O}_4\text{Ti}$ in anhydrous ethanol. Then, the prepared AAO templates were dipped into Ti-Nb sol and dried under an vacuum atmosphere to make sure the sol was fully infused into the pores of the templates. Undergone calcinations, the Ti-Nb composites within the walls of the templates were *in situ* converted into TiNb_2O_7 with good crystalline. Finally, the AAO templates were dissolved away by immersion in concentrated H_3PO_4 solution, resulting in the 3D-O-P-TNO. The phase purity and structural characterization of the 3D-O-P-TNO is provided in Fig. 2. X-ray diffraction (XRD) results (Fig. 2a) indicated that all of the diffraction peaks of the 3D-O-P-TNO specimen could be indexed to the monoclinic structure form of TiNb_2O_7 (space group: $\text{C}2/m$, JCPDS#: 39-1407). It is generally believed that the Ti and Nb metal atom is coordinated with six oxygen atoms forming an octahedral group. The crystallographic-shear framework structure is built by edge and corner sharing octahedral connected with each other, as illustrated in Fig. 2b. It should be noted that the calcination temperature we used is 700°C which is crucial for the etching of Al_2O_3 . According to the research by Cui's group, the AAO template heated to above 780°C was hard to remove due to the amorphous Al_2O_3 could be converted to a crystalline phase.⁴⁴ Fig. 2c is the SEM image of the 3D-O-P-TNO which reveals the hollow tubular morphology. For comparison, the morphology of the bulk TNO was also characterized which was shown in Fig. S1. The TEM image of the 3D-O-P-TNO shown in Fig. 2d further exhibits that the diameter of the as-prepared products is about 200 nm. Fig. 2e and 2f shows the high-resolution TEM (HRTEM) images, revealing that an interesting porous structure has formed and distributed highly uniform throughout the length of the tubes. The similar nanoporous structure could be seen in the reference reported by Guo *et al.* However, the surfactant Block-copolymer F127 was a necessity to built such architecture.²⁷ The inset in Fig. 2f shows the selected area electron diffraction (SAED) pattern of 3D-O-P-TNO which exhibits a polycrystalline nature. The elemental mapping images (Fig. S2) confirm the uniform distribution of Ti, Nb, and O. Nitrogen adsorption/desorption isotherms were further measured to characterize the porous structure of the products. The Brunauer-Emmerr-Teller (BET) surface area of 3D-O-P-TNO was $50.2\text{ m}^2\text{ g}^{-1}$ and the nitrogen adsorption/desorption isotherms was corresponded to be type IV

35

40

45

50

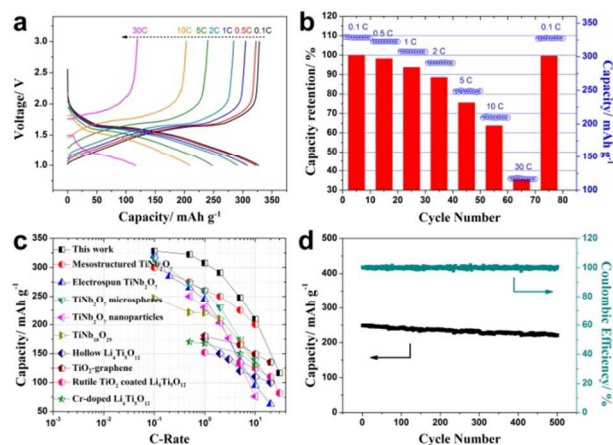


Fig. 3. Electrochemical characteristics of 3D-O-P-TNO: (a) The charge/discharge curves at different current rates; (b) The capacity retention and cycling performances of 3D-O-P-TNO at different rates; (c) Comparison of rate capability of 3D-O-P-TNO with other Ti-based high rate electrodes reported recently; (d) Cycling performances of 3D-O-P-TNO at the rate of 5 C.

curves with the H3 hysteresis loops (Fig. S3a).^{45, 46} The Barret-Joyner-Halenda (BJH) pore-size distribution curve (Fig. S3b) indicated that the pore sizes in 3D-O-P-TNO were mainly below 20 nm with pore volume of $0.15\text{ cm}^3\text{ g}^{-1}$. While the BET surface area of the bulk TNO was only $16.8\text{ m}^2\text{ g}^{-1}$ (shown in Fig. S4), which is far less than the 3D-O-P-TNO samples.

The Li-insertion properties of 3D-O-P-TNO were investigated using half cells *vs.* Li/Li^+ . Fig. 3a shows the charge/discharge profiles of 3D-O-P-TNO obtained at different current densities. As the current rate increased from 0.1 to 5 and 10 C, the distinguish between the two discharge plateaus gradually becomes blurred and the plateau voltages shift toward lower potentials, and the discharge capacity slightly decreased from 328.3 to 248.1 and 209.3 mAh g^{-1} , respectively. Even at a very high rate of 30 C, the capacity still retained 116.6 mAh g^{-1} , indicating the excellent rate capability of the 3D-O-P-TNO electrode. Fig. 3b shows that the 3D-O-P-TNO displays an excellent steady capacity and high capacity retention at every rate test. Noted that the capacity retention at 10 C is as high as 63.75% compared with the value at 0.1 C (defined as 100%). In comparison, the bulk TNO was also tested using the same method which was shown in Fig. S5. Obviously, the discharge capacity of bulk TNO electrodes was dramatically faded with the values of 283.1 mAh/g at 0.1 C, and only 96.7 mA h/g at 5 C. Furthermore, the capacity retention at 5 C is only 34.16% compared with the value at 0.1 C (defined as 100%), which is far inferior than it (75.57%) obtained from the 3D-O-P-TNO. To clarify the improved electrochemical properties of 3D-O-P-TNO, Electrochemical Impedance Spectroscopy (EIS) were carried out for both the prepared samples as shown in the Fig. S6. Clearly, all spectra consist of a depressed semicircle in the high-frequency region and an oblique straight line in the low-frequency region. Moreover, the diameter of the semicircles for the 3D-O-P-TNO electrode was much smaller than that of the bulk TNO electrode. This result obviously validates that the well designed three-dimensional porous architecture of TiNb_2O_7 nanotubes electrode possesses lower contact and charge-transfer impedance. We also

75

80

85

90

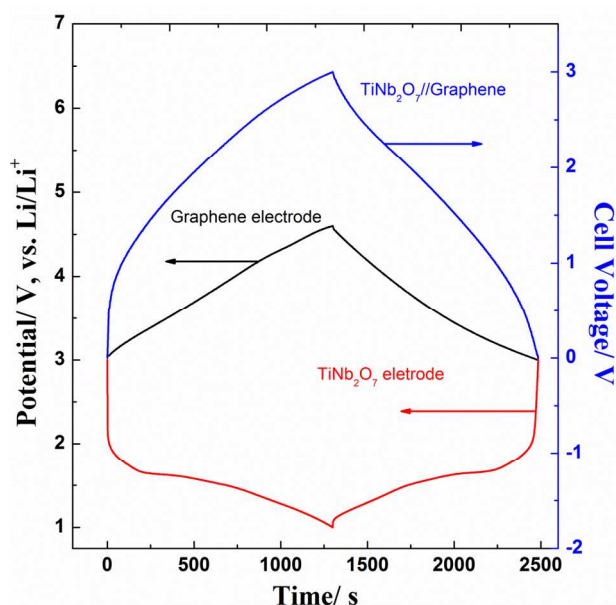


Fig. 4. Galvanostatic charge/discharge curves of the individual composite electrode (3D-O-P-TNO and graphene grass) vs. Li/Li^+ reference electrode, along with the voltage profile of the 3D-O-P-TNO/graphene grass hybrid supercapacitor.

compared the current work with other Ti-based high rate electrodes reported in the recent work^{28, 30, 32, 47-52} and these results are shown in Fig. 3c. The long-term cycling performance of the 3D-O-P-TNO and corresponding Coulombic efficiency at a charge/discharge rate of 5 C are displayed in Fig. 3d. Over the whole 500 cycles, superior cycling performance is observed for this high C-rate characterized by stable discharge capacities of about 235 mAh g^{-1} .

As mentioned above, the 3D-O-P-TNO should be a promising anode material for hybrid supercapacitor. To further explore this application, we assembled a cell based on an anode electrode of 3D-O-P-TNO and a cathode electrode of graphene grass in a non-aqueous electrolyte (see Fig. S7). The morphology characteristics and electrochemical properties of our prepared graphene grass were tested in advance to estimate the optimum mass loading between the two electrodes, which were shown in Fig. S8 and Fig. S9. Fig. 4 shows the galvanostatic charge/discharge curves of the individual composite electrode (3D-O-P-TNO and graphene grass) vs. Li/Li^+ reference electrode, along with the voltage profile of the 3D-O-P-TNO/graphene grass hybrid supercapacitor at a current density of 0.15 A g^{-1} . As shown in Fig. 4, the operating potential window of the cathode electrode of graphene grass in the potential region from 3.0 to 4.6 V, coupled with PF_6^- anion adsorption/desorption. During the electrochemical reaction, a linear increase in potential with respect to time, which suggests the good absorption/desorption of PF_6^- and subsequent double layer formation across the electrode/electrolyte interface.⁵³ The anode electrode of 3D-O-P-TNO charged/discharged in the potential region from 1.0 to 3.0 V. Furthermore, it can also be observed that the 3D-O-P-TNO/graphene grass hybrid supercapacitor exhibited a slop voltage profile from 0 to 3 V, resulting from the difference between the cathode electrode of

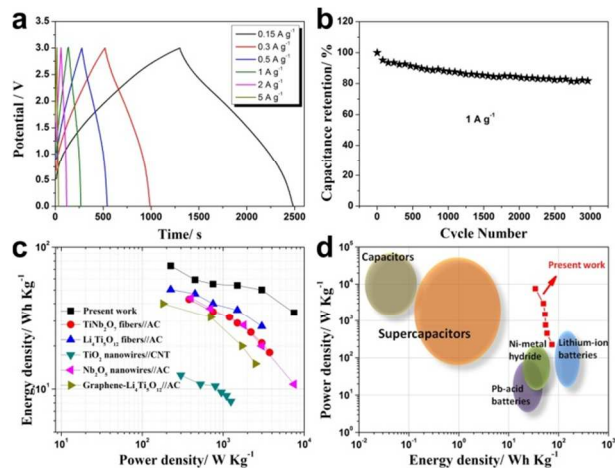


Fig. 5. (a) Galvanostatic charge/discharge curves of $\text{TiNb}_2\text{O}_7//\text{Graphene}$ hybrid supercapacitor at different current densities; (b) Relationship between cycle number and capacitance retention and coulombic efficiency at 1 A g^{-1} ; (c) Ragone plot of $\text{TiNb}_2\text{O}_7//\text{Graphene}$ hybrid supercapacitor and comparison with recent literature data; (d) Ragone plots for the $\text{TiNb}_2\text{O}_7//\text{Graphene}$ hybrid supercapacitor and other typical electrical energy storage devices.

graphene grass and the anode electrode of 3D-O-P-TNO.

Fig. 5a shows the galvanostatic charge/discharge curves of 3D-O-P-TNO/graphene grass at various current densities (the applied current density is based on the total mass of the active material used in both electrodes). It is evident that the hybrid supercapacitors exhibit a deviation from the well-symmetric triangle shape which further demonstrates that the energy storage mechanism is a combination of redox reactions and surface adsorption/desorption processes. During the charging process, monoclinic TiNb_2O_7 anode undergoes reversible Li-insertion whereas the graphene cathode involves electric double layer formation with PF_6^- anions across the electrode/electrolyte interface. The aforementioned reaction is reversed during the discharging process. Furthermore, the $\text{TiNb}_2\text{O}_7//\text{Graphene}$ hybrid supercapacitor can finish charge/discharge within 35 seconds at the current density of 5 A g^{-1} , displaying excellent power performance. Fig. 5b reveals the outstanding cycle stability of the $\text{TiNb}_2\text{O}_7//\text{Graphene}$ hybrid supercapacitor up to 3000 times. It can be detected that the capacitance retention could be able to stabilize at 81.25%, corresponding to 0.0062% capacity fading per cycle.

The Ragone plot (energy density vs. power density) of the $\text{TiNb}_2\text{O}_7//\text{Graphene}$ hybrid supercapacitor is presented in Fig. 5c, the energy and power density are calculated from the following formulae given in the literature.⁵⁴

$$E = \int_{t_1}^{t_2} IV dt = \frac{1}{2} C (V_{\max} + V_{\min}) (V_{\max} - V_{\min}) \quad (1)$$

where V_{\max} and V_{\min} are respectively the potential at end and beginning of charge curves during galvanostatic measurements, C is the capacitance (F g^{-1}) of hybrid supercapacitor which can be calculated according to Equation (2):

$$C = \frac{I \times t}{m \times \Delta V} \quad (2)$$

In which I is charge/discharge current, t is the discharge time (s), m is the total mass of active material within both electrodes, and ΔV is the different value of the V_{max} and V_{min} .

The power density can be calculated according to Equation (1) and (3):

$$P = \frac{E}{t} \quad (3)$$

From the above calculations, a maximum energy density of $\sim 74 \text{ Wh kg}^{-1}$ is observed for the TiNb_2O_7 //Graphene hybrid supercapacitor, which is much higher than other hybrid systems like TiNb_2O_7 fibers//AC supercapacitors ($\sim 43 \text{ Wh kg}^{-1}$)²², $\text{Li}_4\text{Ti}_5\text{O}_{12}$ fibers//AC supercapacitors ($\sim 50.3 \text{ Wh kg}^{-1}$)⁵⁵, TiO_2 nanowires//CNT supercapacitors ($\sim 12.5 \text{ Wh kg}^{-1}$)¹³, Nb_2O_5 nanowires//AC supercapacitors ($\sim 44 \text{ Wh kg}^{-1}$)⁵⁶, and Graphene- $\text{Li}_4\text{Ti}_5\text{O}_{12}$ //AC supercapacitors ($\sim 40 \text{ Wh kg}^{-1}$)¹⁴. Moreover, our TiNb_2O_7 //Graphene hybrid supercapacitor also shows superior power density compared with other hybrid devices. Fig. 5d shows that the energy density of the TiNb_2O_7 //Graphene hybrid supercapacitor is highly competitive to the supercapacitors and the power density is much higher than the LIBs, simultaneously.

Conclusions

In conclusion, this paper addressed the issues of the direct synthesis of 3D ordered porous TiNb_2O_7 nanotubes *via* facile steps templated process. The TiNb_2O_7 nanotubes with tailored architecture yield high performance battery components and delivered the maximum specific capacitance of 328.3 mAh g^{-1} at 0.1 C in organic electrolyte. A novel hybrid supercapacitor based on the TiNb_2O_7 nanotubes electrode (anode) and graphene grass electrode (cathode) was successfully constructed and evaluated. A high energy density of $\sim 74 \text{ Wh kg}^{-1}$ was achieved and it could maintain as much as $\sim 34.5 \text{ Wh kg}^{-1}$ at a power of 7500 W kg^{-1} . This level of electrochemical performance could potentially bridge the gap between conventional LIBs and supercapacitors. Further, this approach can be readily engineered to fabricate other electrode materials for energy storage applications.

Acknowledgements

This work is financially supported by the National Program on Key Basic Research Project of China (973 Program, No. 2014CB239701), National Natural Science Foundation of China (No. 21173120, 51372116), Natural Science Foundations of Jiangsu Province (No. BK2011030), Funding for Outstanding Doctoral Dissertation in NUAA (BCXJ14-10), Funding of Jiangsu Innovation Program for Graduate Education (KYLX_0255), Fundamental Research Funds for the Central Universities and the Priority Academic Program Development of Jiangsu Higher Education Institutions.

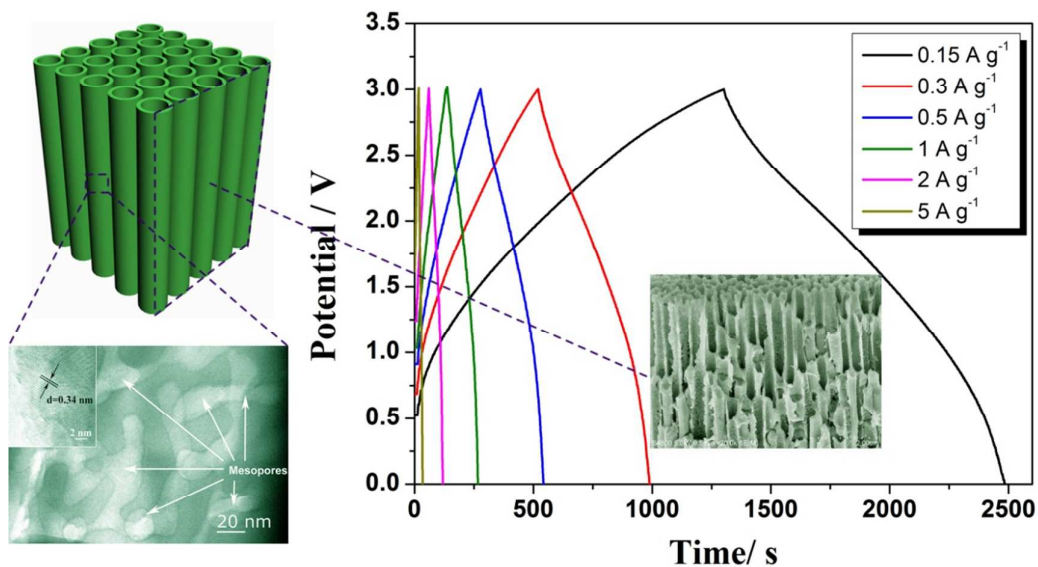
Notes and references

College of Materials Science and Engineering, Key Laboratory of Materials and Technologies for Energy Conversion, Nanjing University of Aeronautics and Astronautics, 29 Yudao road, Nanjing, 210016, P. R. China. Email: a Zhangxg@nuaa.edu.cn

† Electronic Supplementary Information (ESI) available: [SEM, BET, Electrochemical performance and Nyquist plots of the bulk TNO, EDX elemental mapping and Nyquist plots of the 3D-O-P-TNO, schematic

- illustration of the fabricated hybrid supercapacitor, SEM, TEM and electrochemical data of the graphene grass]. See DOI:10.1039/b000000x/
1. J. M. Tarascon and M. Armand, *Nature*, 2001, **414**, 359-367.
 2. F. Bonaccorso, L. Colombo, G. Yu, M. Stoller, V. Tozzini, A. C. Ferrari, R. S. Ruoff, V. Pellegrini, *Science*, 2015, **347**, 1246501-1246509.
 3. Z. Y. Wang, Y. F. Dong, H. J. Li, Z. B. Zhao, H. B. Wu, C. Hao, S. H. Liu, J. S. Qiu and X. W. Lou, *Nat. Commun.*, 2014, **5**.
 4. Z. W. Seh, J. H. Yu, W. Y. Li, P. C. Hsu, H. T. Wang, Y. M. Sun, H. B. Yao, Q. F. Zhang and Y. Cui, *Nat. Commun.*, 2014, **5**.
 5. L. Q. Mai, X. C. Tian, X. Xu, L. Chang and L. Xu, *Chem. Rev.*, 2014, **114**, 11828-11862.
 6. N. S. Choi, Z. H. Chen, S. A. Freunberger, X. L. Ji, Y. K. Sun, K. Amine, G. Yushin, L. F. Nazar, J. Cho and P. G. Bruce, *Angew. Chem. Int. Edit.*, 2012, **51**, 9994-10024.
 7. M. Fehse, E. Ventosa, *ChemPlusChem*, 2015, **80**, 785-795.
 8. P. Xiong, L. Peng, D. Chen, Y. Zhao, X. Wang and G. Yu, *Nano Energy*, 2015, **12**, 816-823.
 9. H. Kim, K. Y. Park, J. Hong and K. Kang, *Sci. Rep.*, 2014, **4**, 5278-5286.
 10. F. Zhang, T. F. Zhang, X. Yang, L. Zhang, K. Leng, Y. Huang and Y. S. Chen, *Energy Environ. Sci.*, 2014, **7**, 3086-3086.
 11. A. Vlad, N. Singh, J. Rolland, S. Melinte, P. M. Ajayan and J. F. Gohy, *Sci. Rep.*, 2014, **4**, 4315-4322.
 12. B. G. Choi, M. Yang, W. H. Hong, J. W. Choi and Y. S. Huh, *ACS Nano*, 2012, **6**, 4020-4028.
 13. Q. Wang, Z. H. Wen and J. H. Li, *Adv. Funct. Mater.*, 2006, **16**, 2141-2146.
 14. H. Kim, K. Y. Park, M. Y. Cho, M. H. Kim, J. Hong, S. K. Jung, K. C. Roh and K. Kang, *ChemElectroChem*, 2014, **1**, 125-130.
 15. K. Leng, F. Zhang, L. Zhang, T. F. Zhang, Y. P. Wu, Y. H. Lu, Y. Huang and Y. S. Chen, *Nano Res.*, 2013, **6**, 581-592.
 16. H. Wang, C. Guan, X. Wang and H. J. Fan, *Small*, 2015, **11**, 1470-1477.
 17. K. Naoi, W. Naoi, S. Aoyagi, J. Miyamoto and T. Kamino, *Acc. Chem. Res.*, 2013, **46**, 1075-1083.
 18. J. T. Zhang and X. S. Zhao, *ChemSusChem*, 2012, **5**, 818-841.
 19. V. Aravindan, J. Gnanaraj, Y.-S. Lee and S. Madhavi, *Chem. Rev.*, 2014, **114**, 11619-11635.
 20. A. Nagasubramanian, A. Jain, A. Vanchiappan, J. Sundaramurthy, W. C. Ling, M. P. Srinivasan and M. Srinivasan, *Nano Energy*, 2014, **12**, 69-75.
 21. G. H. Yu, X. Xie, L. J. Pan, Z. N. Bao and Y. Cui, *Nano Energy*, 2013, **2**, 213-234.
 22. V. Aravindan, J. Sundaramurthy, A. Jain, P. S. Kumar, W. C. Ling, S. Ramakrishna, M. P. Srinivasan and S. Madhavi, *ChemSusChem*, 2014, **7**, 1858-1863.
 23. Z. L. Wang, R. Guo, L. X. Ding, Y. X. Tong and G. R. Li, *Sci. Rep.*, 2013, **3**, 1204-1211.
 24. K. H. An, W. S. Kim, Y. S. Park, J. M. Moon, D. J. Bae, S. C. Lim, Y. S. Lee and Y. H. Lee, *Adv. Funct. Mater.*, 2001, **11**, 387-392.
 25. M. Winter and R. J. Brodd, *Chem. Rev.*, 2005, **105**, 1021-1021.
 26. R. Gokhale, V. Aravindan, P. Yadav, S. Jain, D. Phase, S. Madhavi and S. Ogale, *Carbon*, 2014, **80**, 462-471.

27. B. K. Guo, X. Q. Yu, X. G. Sun, M. F. Chi, Z. A. Qiao, J. Liu, Y. S. Hu, X. Q. Yang, J. B. Goodenough and S. Dai, *Energy Environ. Sci.*, 2014, **7**, 2220-2226.
28. C. Jo, Y. Kim, J. Hwang, J. Shim, J. Chun and J. Lee, *Chem. Mater.*, 2014, **26**, 3508-3514.
29. J. T. Han, Y. H. Huang and J. B. Goodenough, *Chem. Mater.*, 2011, **23**, 2027-2029.
30. L. Fei, Y. Xu, X. F. Wu, Y. L. Li, P. Xie, S. G. Deng, S. Smirnov and H. M. Luo, *Nanoscale*, 2013, **5**, 11102-11107.
31. S. Jayaraman, V. Aravindan, P. S. Kumar, W. C. Ling, S. Ramakrishna and S. Madhavi, *ACS Appl. Mater. Inter.*, 2014, **6**, 8660-8666.
32. H. Li, L. Shen, G. Pang, S. Fang, H. Luo, K. Yang and X. Zhang, *Nanoscale*, 2015, **7**, 619-624.
33. H. Park, H. B. Wu, T. Song and U. Paik, *Adv. Energy Mater.*, 2015, DOI: 10.1002/aenm.201401945.
34. C. Lin, S. Yu, S. Wu, S. Lin, Z.-Z. Zhu, J. Li and L. Lu, *J. Mater. Chem. A*, 2015, **3**, 8627-8635.
35. H. Park, T. Song, U. Paik, *J. Mater. Chem. A*, 2015, **3**, 8590-8596.
36. J. Z. Wang, N. Du, H. Zhang, J. X. Yu and D. R. Yang, *J. Phys. Chem. C*, 2011, **115**, 11302-11305.
37. Z. Favors, W. Wang, H. H. Bay, A. George, M. Ozkan and C. S. Ozkan, *Sci. Rep.*, 2014, **4**, 4605-4611.
38. J. Liu, K. P. Song, P. A. van Aken, J. Maier and Y. Yu, *Nano Lett.*, 2014, **14**, 2597-2603.
39. T. Brezesinski, J. Wang, S. H. Tolbert and B. Dunn, *Nat. Mater.*, 2010, **9**, 146-151.
40. B. Z. Tian, P. Xie, T. J. Kempa, D. C. Bell and C. M. Lieber, *Nat. Nanotechnol.*, 2009, **4**, 824-829.
41. K. Dai, L. H. Lu, Q. Liu, G. P. Zhu, X. Q. Wei, J. Bai, L. L. Xuan and H. Wang, *Dalton Trans.*, 2014, **43**, 6295-6299.
42. X. J. Lu, H. Dou, C. Z. Yuan, S. D. Yang, L. Hao, F. Zhang, L. F. Shen, L. J. Zhang and X. G. Zhang, *J. Power Sources*, 2012, **197**, 319-324.
43. K. Momma and F. Izumi, *J. Appl. Crystallogr.*, 2008, **41**, 653-658.
44. G. Y. Zheng, Y. Yang, J. J. Cha, S. S. Hong and Y. Cui, *Nano Lett.*, 2011, **11**, 4462-4467.
45. Q. L. Wei, Q. Y. An, D. D. Chen, L. Q. Mai, S. Y. Chen, Y. L. Zhao, K. M. Hercule, L. Xu, A. Minhas-Khan and Q. J. Zhang, *Nano Lett.*, 2014, **14**, 1042-1048.
46. Q. Y. An, F. Lv, Q. Q. Liu, C. H. Han, K. N. Zhao, J. Z. Sheng, Q. L. Wei, M. Y. Yan and L. Q. Mai, *Nano Lett.*, 2014, **14**, 6250-6256.
47. K. Tang, X. K. Mu, P. A. van Aken, Y. Yu and J. Maier, *Adv. Energy Mater.*, 2013, **3**, 49-53.
48. X. Y. Wu, J. Miao, W. Z. Han, Y. S. Hu, D. F. Chen, J. S. Lee, J. Kim and L. Q. Chen, *Electrochem. Commun.*, 2012, **25**, 39-42.
49. L. Yu, H. B. Wu and X. W. Lou, *Adv. Mater.*, 2013, **25**, 2296-2300.
50. N. Li, G. Liu, C. Zhen, F. Li, L. L. Zhang and H. M. Cheng, *Adv. Funct. Mater.*, 2011, **21**, 1717-1722.
51. Y. Q. Wang, L. Guo, Y. G. Guo, H. Li, X. Q. He, S. Tsukimoto, Y. Ikuhara and L. J. Wan, *J. Am. Chem. Soc.*, 2012, **134**, 7874-7879.
52. H. Song, S. W. Yun, H. H. Chun, M. G. Kim, K. Y. Chung, H. S. Kim, B. W. Cho and Y. T. Kim, *Energy Environ. Sci.*, 2012, **5**, 9903-9913.
53. E. Frackowiak and F. Beguin, *Carbon*, 2001, **39**, 937-950.
54. Y. G. Wang, Z. S. Hong, M. D. Wei and Y. Y. Xia, *Adv. Funct. Mater.*, 2012, **22**, 5185-5193.
55. H. H. Xu, X. L. Hu, Y. M. Sun, W. Luo, C. J. Chen, Y. Liu and Y. H. Huang, *Nano Energy*, 2014, **10**, 163-171.
56. X. Wang, C. Yan, J. Yan, A. Sumboja and P. S. Lee, *Nano Energy*, 2014, **11**, 765-772.



A novel hybrid supercapacitor is successfully constructed based on the 3D ordered porous TiNb_2O_7 electrode (anode) and graphene grass electrode (cathode). In combination with the advantages from the lithium ion batteries and supercapacitors, this device shows superior energy density and power density with improved cycling performances, offering a feasible solution to create the next generation hybrid supercapacitors.